RSC Advances

PAPER

View Article Online
View Journal | View Issue

Cite this: *RSC Adv.*, 2018, **8**, 5441

Fabrication and photocatalytic property of magnetic $SrTiO_3/NiFe_2O_4$ heterojunction nanocomposites

Yongmei Xia,[a] Zuming He, *[b] Yalin Lu,[a] Bin Tang,[c] Shunping Sun,[a] Jiangbin Su [c] and Xiaoping Li[a]

Received 13th November 2017
Accepted 26th January 2018

DOI: 10.1039/c7ra12393k

rsc.li/rsc-advances

Novel multifunctional $SrTiO_3/NiFe_2O_4$ nanocomposites were successfully fabricated *via* a two-step route. The as-prepared samples were characterized by using X-ray diffraction (XRD), field-emission scanning electron microscopy (FESEM), energy dispersive spectroscopy (EDS), field-emission transmission electron microscopy (TEM), UV-visible diffuse reflectance spectroscopy (DRS), X-ray photoelectron spectroscopy (XPS), photoluminescence (PL) spectroscopy and vibrating sample magnetometry (VSM). The results indicate that the $SrTiO_3/NiFe_2O_4$ heterostructures are composed of $SrTiO_3$ spheroidal nanoparticles adhered to $NiFe_2O_4$ polyhedra. The heterojunction established in the composite material accelerates the process of electron–hole pair separation and boosts the photo-Fenton reaction. Among the samples, 15 wt% $SrTiO_3/NiFe_2O_4$ nanocomposites exhibit a powerful light response and excellent room temperature ferromagnetism. Subsequently, the photocatalytic degradation of RhB over the as-prepared samples was investigated and optimized, revealing that the 15 wt% $SrTiO_3/NiFe_2O_4$ nanocomposites exhibit the best photocatalytic activity and stability under simulated solar light irradiation. Furthermore, according to experimental results, the possible mechanism of improved photocatalytic activity was also proposed.

1. Introduction

Photocatalysis has attracted researchers' interest due to its potential application in degradation of organic compounds for wastewater treatment, water splitting to produce high purity hydrogen, solar panels, and so on.[1–4] Several photocatalytic semiconductor materials, for instance ZnO and TiO_2, have been widely used in degradation of organic compounds, nevertheless, most photocatalysts are faced with two problem: low efficiency under visible-light irradiation and difficult recycling of photocatalysts after use. Thus, development of magnetic and highly efficient visible-light-driven photocatalysts has become an appealing challenge. Recent investigation of magnetic semiconductor photocatalysts has attracted attention due to their easy recycling, such as MFe_2O_4 (M = Ni, Zn, Fe, Co, Cu). Among these well-known magnetic semiconductors, $NiFe_2O_4$ is a visible-light response semiconductor material, typical representative of magnetic materials with high stability, high magnetic permeability and high electrical resistivity. It has wide application for magnetic devices, catalysis, water treatment, magnetic fluids and microwave absorbing materials.[5–8] Unfortunately, pure $NiFe_2O_4$ exhibits lower photocatalytic activity owing to fast recombination of photoelectron–hole pairs.[9,10] To improve the photocatalytic activity, many researchers have reported combinations with other semiconductor materials and doping to solve the problem meaningfully. Such as, Ji and Jing synthesized the magnetic g-$C_3N_4/NiFe_2O_4$ hybrids by a facile chemisorption method to degrade methyl orange dye,[11] Zeng and Song synthesized the Au/g-$C_3N_4/NiFe_2O_4$ nanocomposites by a facile calcination method for enhanced visible-light-driven photocatalytic hydrogen evolution[12], Dongdong Lv, *et al.* synthesized magnetic $NiFe_2O_4$/BiOBr nanocomposites by one-pot combustion for degradation of model dyes MB,[13] Wang and Fu synthesized $NiFe_2O_4$/MWCNT to degrade phenol with C/C_0 reaching 90% in 400 min under UV light,[14] Hua-Yue Zhu, *et al.* synthesized the $NiFe_2O_4$/ZnO hybrids using a hydrothermal method to degrade congo red solution with C/C_0 reaching 94.55% under simulated solar light irradiation for 10 min,[15,16] and so on. $SrTiO_3$ is perovskite p-type indirect semiconductor, endowed with corrosion properties, thermal stability, photocatalytic activity.[17,18] However, pure $SrTiO_3$ is used for dye degradation only in the UV region due to its wide band gap of 3.2 eV, consequently limiting its photocatalytic activity to the visible light region of the sunlight spectrum.[19] Besides, pure $SrTiO_3$ photocatalyst is difficult to be separated

[a]Jiangsu Key Laboratory of Advanced Material Design and Additive Manufacturing, School of Materials and Engineering, Jiangsu University of Technology, Changzhou 213001, China

[b]Huaide School, Changzhou University, Jingjiang 214500, China. E-mail: hzm432928@cczu.edu.cn

[c]School of Mathematics & Physics, Changzhou University, Jiangsu 213164, China

and recycled from wastewater and easily produces secondary pollution, which limits the practical application of $SrTiO_3$. To overcome the above problem, many researchers have adopted metal or anion doping and coupling to other semiconductor to enhance the photocatalytic ability of $SrTiO_3$, such as lanthanum and nitrogen-co-doped $SrTiO_3/TiO_2$,[20] Cu-loaded $SrTiO_3$,[21] Cr-doped $SrTiO_3$/g-C_3N_4,[22] g-C_3N_4/N-doped $SrTiO_3$,[23] Rh-doped $SrTiO_3$,[24] Ag_3PO_4/Cr-$SrTiO_3$,[25] $SrTiO_3$/BiOBr,[26] $LaFeO_3/SrTiO_3$ (ref. 27) and Panpan Jing *et al.* synthesized the hierarchical $SrTiO_3/NiFe_2O_4$ porous nanotubes by electrospinning method for degrade methyl orange dye.[28,29] However, the electrospinning method is disadvantaged by high cost and rigorous condition in procedure, and is unsuitable for industrial production. If magnetic $NiFe_2O_4$ nanoparticles are coupled with $SrTiO_3$ by a facile and large-scale preparation method, it is possible to improve the photocatalytic activity and convenient separation from the waste water.

Inspired by the previous studies, we synthesized a series of $SrTiO_3/NiFe_2O_4$ nanocomposites with different percentage of $SrTiO_3$ by a simple two-step method. The photocatalytic performance of the $SrTiO_3/NiFe_2O_4$ nanocomposites catalysts was evaluated by the photodegradation of rhodamine B (RhB) dyes under simulated solar light illumination.

2. Experimental

2.1. Materials

Nickel chloride hexahydrate ($NiCl_2 \cdot 6H_2O \geq 99.5\%$), iron chloride hexahydrate ($FeCl_3 \cdot 6H_2O \geq 99\%$), sodium hydroxide ($NaOH \geq 98.5\%$), strontium chloride ($SrCl_2 \cdot 6H_2O \geq 99.5\%$), acetic acid ($CH_3COOH \geq 99\%$), citric acid ($C_6H_8O_7 \geq 99\%$), titanium isopropoxide ($(CH_3CH_3CHO)4Ti \geq 99.5\%$ were purchased from Aladdin Industrial Co., Ltd (Shanghai, China). All the reagents were of analytical grade and used without any further purification.

2.2. Preparation of $SrTiO_3/NiFe_2O_4$ nanocomposites

2.2.1 Preparation of $SrTiO_3$. $SrTiO_3$ was synthesized by a sol–gel method. In a typical process,[30] 14.2 mL of $(CH_3CH_3CHO)_4Ti$ was dissolved in 24 mL of CH_3COOH, and 20 mL water was added to the $(CH_3CH_3CHO)_4Ti$ solution under magnetic stirring till clear transparent solution was obtained. 12.797 g of $SrCl_2 \cdot 6H_2O$ dissolved in 20 mL of water and 4 M $C_6H_8O_7$ were added to the above solution, and then the pH of the solution was adjusted to 1.5. The solution was stirred for 6 h and heated in waterbath at 65 °C for 8 h. The viscous sol obtained was again heated at 110 °C for 12 h. The brown mass formed was dried at 200 °C for 8 h and heated at 500 °C for 8 h till it changed into white powder.

2.2.2 Preparation of $SrTiO_3/NiFe_2O_4$. First, 0.02 mol $FeCl_3 \cdot 6H_2O$ was dissolved into 150 mL distilled water and 0.01 mol $NiCl_2 \cdot 6H_2O$ was dissolved into the $FeCl_3$ aqueous solution under magnetic stirring. The pH of the solution was adjusted to 13.0 with NaOH solution, and heated in waterbath at 80 °C for 1 h, during which time the red-brown products gradually precipitated from the solution. Second, the pH of the solution was adjusted to 7.0 with distilled water, and then, 0.4136 g $SrTiO_3$ was added to the solution under magnetic stirring. Finally, the products were collected, repeatedly washed with distilled water, and then annealed at 500 °C for 3 h in air. The reddish brown 15 wt% $SrTiO_3/NiFe_2O_4$ powder was obtained. According to this method, other $SrTiO_3/NiFe_2O_4$ photocatalysts with different $SrTiO_3$ content were synthesized. To comparison, pure $NiFe_2O_4$ was obtained without $SrTiO_3$ while keeping all the other conditions unchanged.

2.3. Instruments and characterization

X-ray powder diffraction (XRD) patterns were recorded with an X-ray diffractometer model D/max-2500 (Rigaku, Japan) with Cu Kα radiation ($\lambda = 1.5418$ Å). The diffractometer was set at 40 kV accelerating voltage and 20 mA applied current, and the samples were scanned from 10° to 80° at a rate of 0.02° s^{-1}. The morphology and average grain size of the samples were observed using field emission scanning electron microscopy (FESEM, SUAPR55, Zeiss, Germany) equipped with energy dispersive X-ray spectroscopy (EDS). The microscopic features of the samples were characterized by transmission electron microscopy (TEM, FEI Tecnai F20). X-ray photoelectron spectroscopy (XPS) data were collected from a ESCALAB 250Xi X-ray photoelectron spectrometer from VG Scientific using 300 W Al Kα radiation (Thermo Fisher Scientific, USA). The UV-vis diffuse reflectance spectra (DRS) were obtained using a UV-9000S UV-vis spectrophotometer (METASH, China). The photoluminescence (PL) spectra of samples were measured by a FLs980 fluorescence spectrophotometer (Edinburgh, UK). The magnetism of the composites was analyzed on a MPMS XL-7 magnetometer (Quantum Design, USA).

2.4. Evaluation of photocatalytic performance

The photocatalytic performances of all the as-synthesized catalysts were assessed by degradation of target pollutants RhB solution under simulated solar light illumination. The photodegradation experiments were done according to procedures described by us in previous report.[31] The specific process is as follows: 100 mg photocatalyst was added into the RhB solution (20 mg L^{-1}, 100 mL), which was stirred in the dark for 30 min. The RhB solution was put in the photocatalytic experiment device, where the 0.4 mW cm^{-2} light intensity was ensured. During each photocatalytic experiment, 5 mL of the sample suspension was taken out at certain time intervals and separated to remove the residual particles. Residual RhB solution concentrations were analyzed by measuring the absorbance peak at 554 nm with the UV-9000S UV-vis spectrometer at ambient temperature, respectively. The degradation efficiency η (%) of dye solution can be calculated according to eqn (1)

$$\eta(\%) = [(A_0 - A_t)]/A_0 \times 100\% \quad (1)$$

where η (%) is the degradation rate of the dye (catalytic degradation at any time t (min), A_0 is the initial absorbance of the dye solution, and A_t is the absorbance of the dye solution at degradation time t (min).

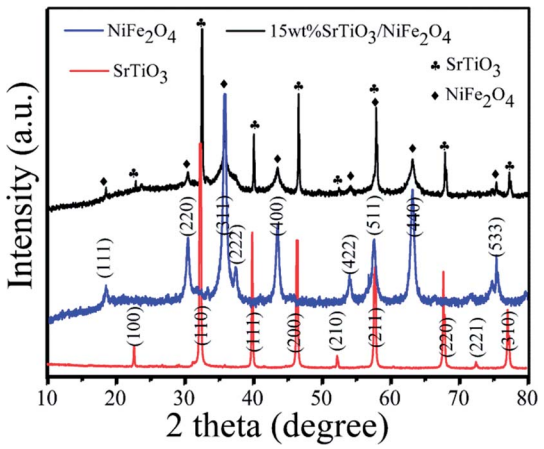

Fig. 1 XRD patterns of pure $SrTiO_3$, pure $NiFe_2O_4$ and 15 wt% $SrTiO_3$/$NiFe_2O_4$ nanocomposites.

3. Results and discussion

3.1. XRD analysis

The XRD patterns of as-synthesized samples are presented in Fig. 1. For the XRD pattern of the pure $SrTiO_3$, all the diffraction peaks at the 2θ values of 22.75°, 32.39°, 39.95°, 46.47°, 52.34°, 57.78°, 67.82°, 72.56° and 77.18° can be indexed to (100), (110), (111), (200), (210), (211), (220), (221) and (310) crystal planes of perovskite $SrTiO_3$ (JCPDS no. 73-0661), respectively.[32] Besides, no evidence of other impurities is found. From the XRD pattern of pure $NiFe_2O_4$, it can be seen that the diffraction peaks can be indexed to spinel crystals $NiFe_2O_4$ (JCPDS no. 54-0964).[33,34] All the diffraction peaks of $NiFe_2O_4$ at the 2θ values of 18.39°, 30.28°, 35.68°, 37.33°, 43.37°, 53.82°, 63.10° 67.33°and 74.58° are corresponded to (111), (220), (311), (222), (400), (422), (511), (440), and (533) crystal planes, respectively. From the XRD pattern of the 15 wt% $NiFe_2O_4$/$SrTiO_3$ nanocomposites, it found that the (100), (110), (111), (200), (210), (211), (220), (221) and (310) peaks correspond to $SrTiO_3$ phase and the (111), (220), (311), (222), (400), (422), (511), (440) and (533) peaks conform to spinel $NiFe_2O_4$ phase. No other impurities are observed.

3.2. XPS analysis

To investigate the elemental composition and chemical states of the as-prepared samples, XPS measurement was carried out to characterize the 15 wt% $SrTiO_3$/$NiFe_2O_4$ nanocomposites, and the results are displayed in Fig. 2. The XPS survey scan spectrum of $SrTiO_3$/$NiFe_2O_4$ nanocomposites is shown in Fig. 2a, indicating the existence of Ni, Fe, Sr, Ti and O elements in the composites. Furthermore, all the obtained binding energies were referenced to the C 1s (284.65 eV). Fig. 2b shows the XPS spectrum of Ni 2p, where the two peaks at 854.16 eV and 873.62 eV correspond to the banding energies of Ni $2p_{3/2}$ and Ni $2p_{1/2}$, respectively, which suggests the typical banding energy of Ni^{2+}.[35] Fig. 2c shows the XPS spectrum of Fe 2p. The peak at 710.41 eV corresponds to the binding energy of Fe $2p_{3/2}$, and the peak at 724.72 eV ascribes to Fe $2p_{1/2}$ signal, indicating that the Fe element exists in the Fe^{3+} ions.[36] In the spectrum of Sr 3d (Fig. 2d), the peaks at 132.50 eV and 134.25 eV conform to the binding energies of Sr $3d_{5/2}$ and Sr $3d_{3/2}$, respectively, indicating the existence of the Sr^{2+} state.[37] As displayed in Fig. 2e, the peaks at 457.90 eV and 463.80 eV are observed in the spectrum of Ti 2p, which correspond to the Ti $2p_{3/2}$ and Ti $2p_{1/2}$, respectively, suggesting that the Ti element exists in the Ti^{4+} state. The peaks

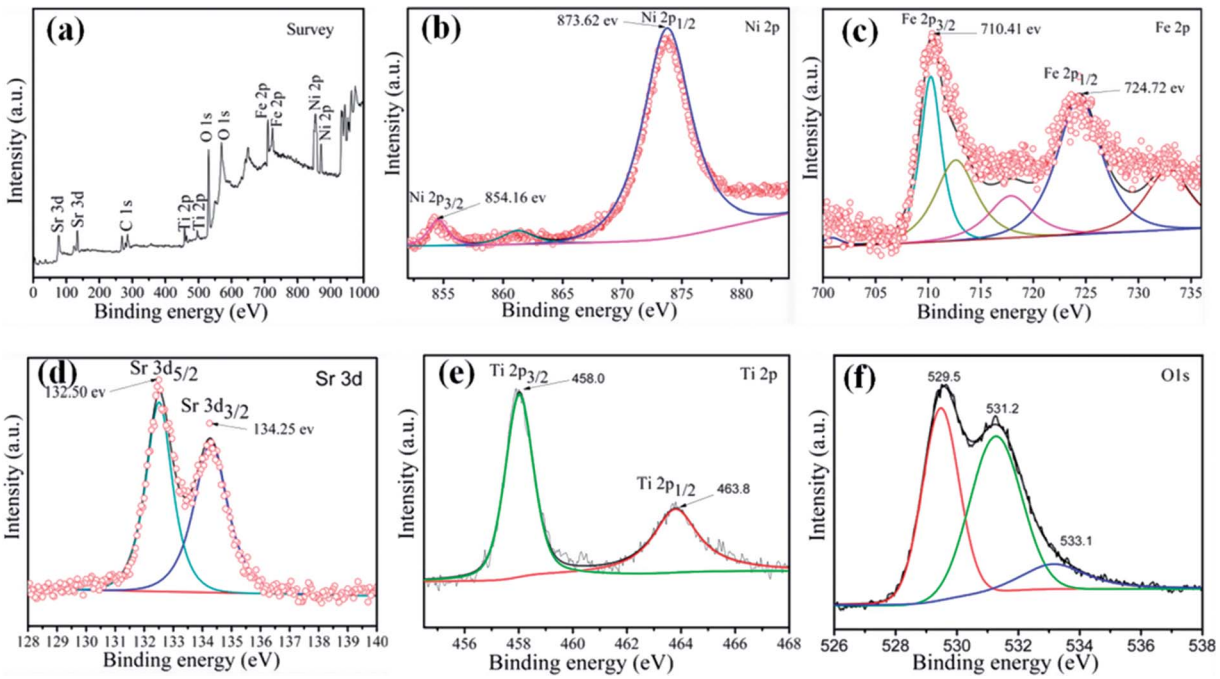

Fig. 2 XPS spectra of the 15 wt% $SrTiO_3$/$NiFe_2O_4$ nanocomposites: the XPS survey spectrum (a), Ni 2p (b), Fe 2p (c), Sr 3d (d), Ti 2p (e) and O 1s (f).

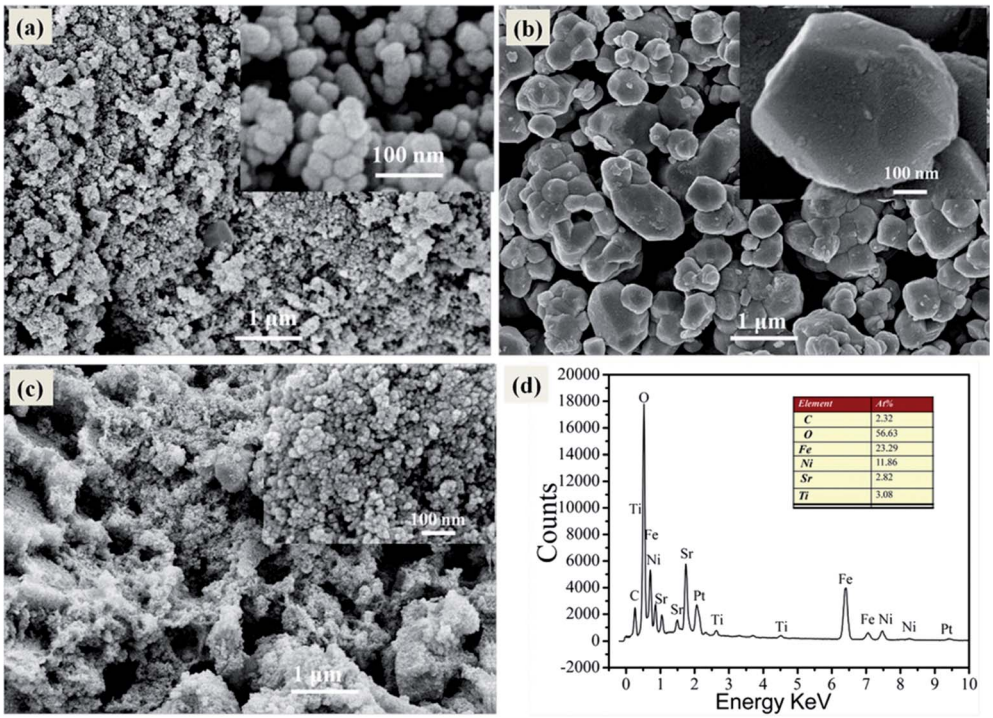

Fig. 3 SEM image of pure $NiFe_2O_4$ (a), pure $SrTiO_3$ (b), 15 wt% $SrTiO_3/NiFe_2O_4$ nanocomposites (c) and EDS spectrum of 15 wt% $SrTiO_3/NiFe_2O_4$ nanocomposites (d).

of O 1s can be divided into three peaks located at 531.2 eV, 529.5 eV and 533.1 eV, revealing three different kinds of O chemical state in the as-prepared samples (Fig. 2f). The peak at 529.5 eV is ascribed to the lattice oxygen of $SrTiO_3/NiFe_2O_4$, the peak at 531.2 eV is generally attributed to the chemisorbed oxygen caused by oxygen vacancies, and the peak at 533.1 eV is

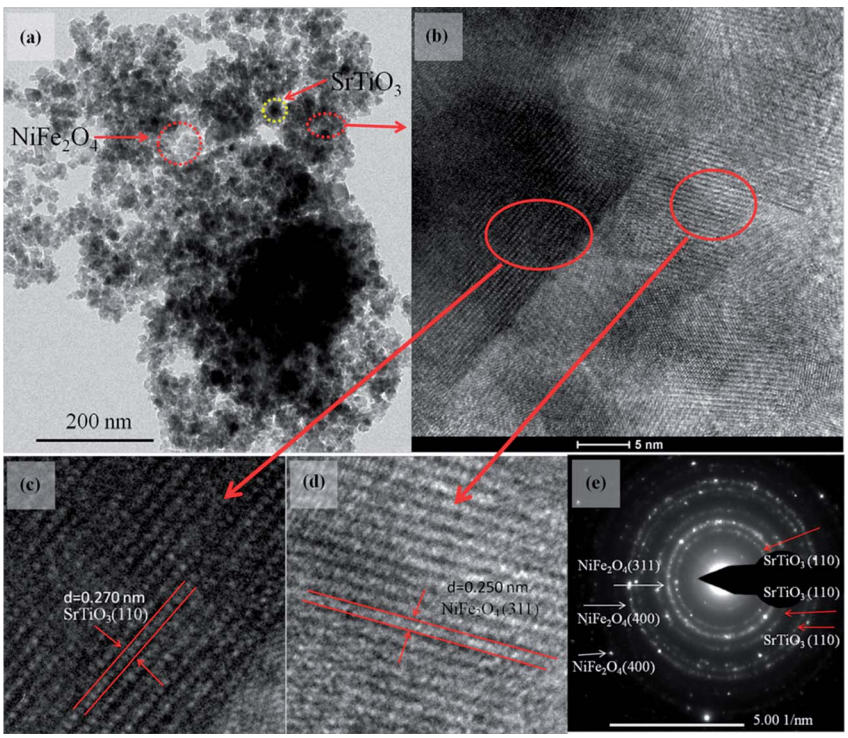

Fig. 4 TEM (a), HRTEM image (b–d) and the SAED pattern (e) for the $SrTiO_3/NiFe_2O_4$ nanocomposites.

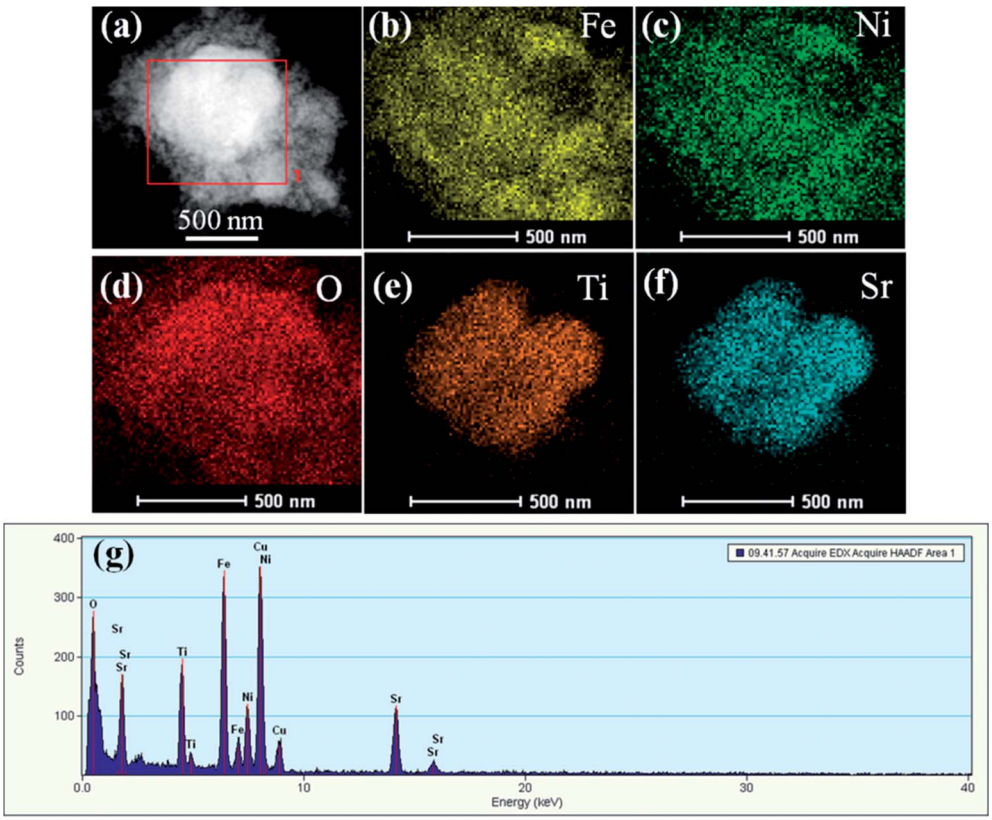

Fig. 5 The corresponding elemental mapping images (a–f) and spot EDS pattern (g) for the $SrTiO_3/NiFe_2O_4$ nanocomposites.

ascribed to the water molecules.[38] The XPS result further confirms the coexistence of $SrTiO_3$ and $NiFe_2O_4$ in the 15 wt% $SrTiO_3/NiFe_2O_4$ nanocomposites.

3.3. SEM and TEM analysis

The particle size and morphology of the samples was investigated by means of SEM, as shown in Fig. 3. In Fig. 3a, it can be clearly observed that the pure $NiFe_2O_4$ is made up of polygon particles with average diameter size about 50 nm. Fig. 3b exhibits the pure $SrTiO_3$ consists of spheroidal or spherical particles with diameters in the range of 300–800 nm. Fig. 2c illustrates that $SrTiO_3$ spheroidal nanoparticles are adhered to the $NiFe_2O_4$ polygon, which would be benefit to form a heterojunction structure and promote the separation efficiency of photoinduced carriers. Furthermore, the as-synthesized 15 wt% $SrTiO_3/NiFe_2O_4$ nanocomposites were analysed by EDS, as shown in Fig. 3d. The elements Fe, Ni, Ti, Sr and O are present in 15 wt% $SrTiO_3/NiFe_2O_4$ nanocomposites, and the atomic ratio is the same as that of stoichiometric composition of the sample.

To get more detailed insight into the microarchitectures of the two $SrTiO_3/NiFe_2O_4$ composites, TEM analysis was further carried out. Fig. 4a shows the TEM image of $SrTiO_3/NiFe_2O_4$ nanocomposites, from which one can see that $NiFe_2O_4$ particles are uniformly dispersed onto the $SrTiO_3$ without any accumulation. Moreover, from the HRTEM image of $SrTiO_3/NiFe_2O_4$ nanocomposites (Fig. 4c and d), it is clearly seen that $SrTiO_3$ and $NiFe_2O_4$ nanoparticles are closely connected to each other. The lattice fringes with a lattice spacing of 0.275 nm and 0.256 nm from different regions could be corresponding to the (110) lattice planes of $SrTiO_3$ and (311) lattice planes of $NiFe_2O_4$, respectively. The SAED pattern (Fig. 4e) contains two sets of diffraction rings, which further indicates the polycrystalline nature of the $SrTiO_3/NiFe_2O_4$ nanocomposites. The first set of diffraction rings (bright circles) composed of bright spots are indexed to the (311), (400) and (440) of $NiFe_2O_4$, while another set (dusky circles) is indexed to the (110), (200) and (211) of $SrTiO_3$. In addition, the elemental mappings are shown in Fig. 5a–f. It can be seen that the signals of Fe, Ni, Sr, Ti and O elements are the same in the spatial distribution. To prove that the $SrTiO_3/NiFe_2O_4$ nanocomposites is a uniform mixture of $SrTiO_3$ and $NiFe_2O_4$ nanoparticles, spot EDS scanning analysis was carried out further, as shown in Fig. 5g. Peaks corresponding to any impurities were found to be absent, peaks corresponding to C and Cu are observed due to the use of carbon coated Cu grids for the analysis.

3.4. UV-vis analysis

Fig. 6a shows the UV-vis diffuse reflectance spectra reflected (DRS) of the pure $NiFe_2O_4$, pure $SrTiO_3$ and $SrTiO_3/NiFe_2O_4$ nanocomposites to reveal their optical properties. The pure $SrTiO_3$ exhibits a 385 nm absorption band-edge in the UV region, corresponding to band gap energy of 3.15 eV.[39,40] The pure $NiFe_2O_4$ absorption band extends to the whole visible-light

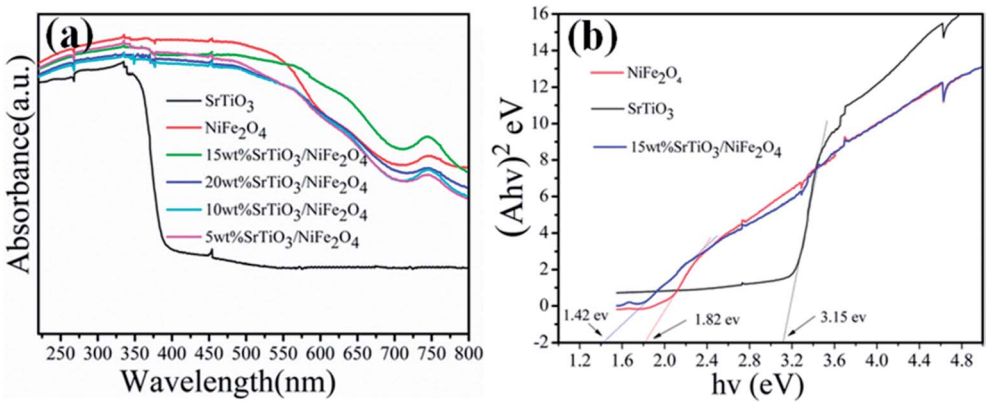

Fig. 6 UV-vis DRS (a) and band gap energy (E_g) (b) of the pure $NiFe_2O_4$, pure$SrTiO_3$ and 15 wt% $SrTiO_3/NiFe_2O_4$ nanocomposite.

region and the absorption peak intensity is more stronger. We also observe that the 15 wt% $SrTiO_3/NiFe_2O_4$ composite has the strongest absorption intensity, which suggests that the integration of $SrTiO_3$ and $NiFe_2O_4$ could promote the photoabsorption ability. Based on the UV-vis DRS results, the bandgaps of the samples can be estimated using Tauc's equation:[41]

$$\alpha h\nu = A\,(h\nu - E_g)^n \quad (2)$$

where α, h, ν, n and A are absorption coefficient, Plank constant, light frequency, the nature of transition and a constant, respectively. Since both $SrTiO_3$ and $NiFe_2O_4$ have the indirect allowed transition, $n = 2$ is substituted in eqn (2). Thus, E_g value of the samples can be estimated from a plot $(\alpha h\nu)^2$ *versus* photon energy ($h\nu$). The intercept of the tangent to X axis would give an approximation of the band gap energy of the sample. From Fig. 6b, the band gap energy of pure $SrTiO_3$, $NiFe_2O_4$ and 15 wt% $SrTiO_3/NiFe_2O_4$ nanocomposites were about 3.15 eV, 1.82 eV and 1.42 eV, respectively, which basically conform to the previous studies.[28,41] The narrowed band gap of 15 wt% $SrTiO_3/NiFe_2O_4$ nanocomposites would enhanced absorption in UV and visible light regions.

3.5. Magnetic properties

Magnetic performance is also very important aspect for magnetic photocatalysts. So the hysteresis loops of pure $NiFe_2O_4$ and 15 wt% $SrTiO_3/NiFe_2O_4$ nanocomposites are shown in Fig. 7. It is seen that the saturation magnetization (M_s) of pour $NiFe_2O_4$ is about 40 emu g^{-1}. Owing to the presence of the non-magnetic $SrTiO_3$, the M_s values for 15 wt% $SrTiO_3/NiFe_2O_4$ nanocomposites, obtained as about 23.35 emu g^{-1}, is lower than that of pure $NiFe_2O_4$. Even so, the 15 wt% $SrTiO_3/NiFe_2O_4$ nanocomposites is adequate to collect and recycle the photocatalyst from the wastewater solution by an external magnetic filed, as shown in the inset of Fig. 6. The results suggest that the 15 wt% $SrTiO_3/NiFe_2O_4$ nanocomposites is an excellent magnetic photocatalysts, which will play an important role in recycling of photocatalysts.

3.6. Photocatalytic performance

RhB is a typical artificial aromatic compound dye with a molecular formula $C_{28}H_{31}ClN_2O_3$ and is commonly used as a colour additive in industry, but it is not easy to decompose by itself. RhB is highly toxic and probably causes cancer.[42] So the degradation of RhB is used to evaluate the photocatalytic performance of the as-prepared pure $NiFe_2O_4$, pure $SrTiO_3$ and $SrTiO_3/NiFe_2O_4$ nanocomposites, as shown in Fig. 8a. It can be seen that the degradation percentage of the dye reaches 38.8%, 47.7%, 59.4%, 84.8%, 97.62%, 74.01% for $NiFe_2O_4$, $SrTiO_3$, 5 wt% $SrTiO_3/NiFe_2O_4$, 10 wt% $SrTiO_3/NiFe_2O_4$, 15 wt% $SrTiO_3/NiFe_2O_4$ and 20 wt% $SrTiO_3/NiFe_2O_4$ under simulated solar light irradiation for 120 min, respectively. In addition, in the absence of photocatalysts, the RhB dye is very stable and its self-decomposition can be neglected. The photocatalytic efficiency of pure $NiFe_2O_4$ in the RhB solution is the lowest, only 38.8% of the dye is observed to be decolorized, which may be ascribed to the fast recombination of photo-generated carriers. These results clearly reveal that 15 wt% $SrTiO_3/NiFe_2O_4$ nanocomposites exhibit the best photocatalytic performance as high as 97.62% under simulated solar light irradiation for 120 min, the photodegradation

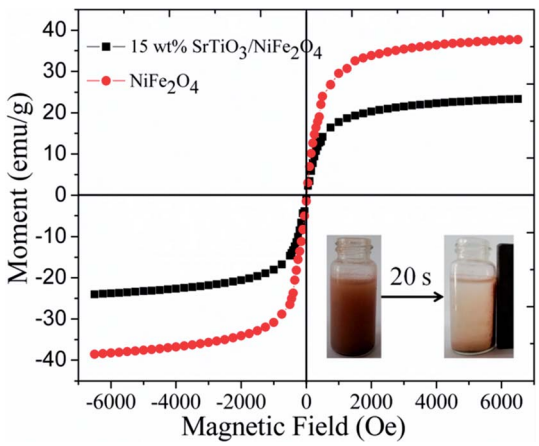

Fig. 7 The hysteresis loops of pure $NiFe_2O_4$ and 15 wt% $SrTiO_3/NiFe_2O_4$ nanocomposite (inset: the magnetic separation of 15-NFO/BOI nanocomposites by a magnet).

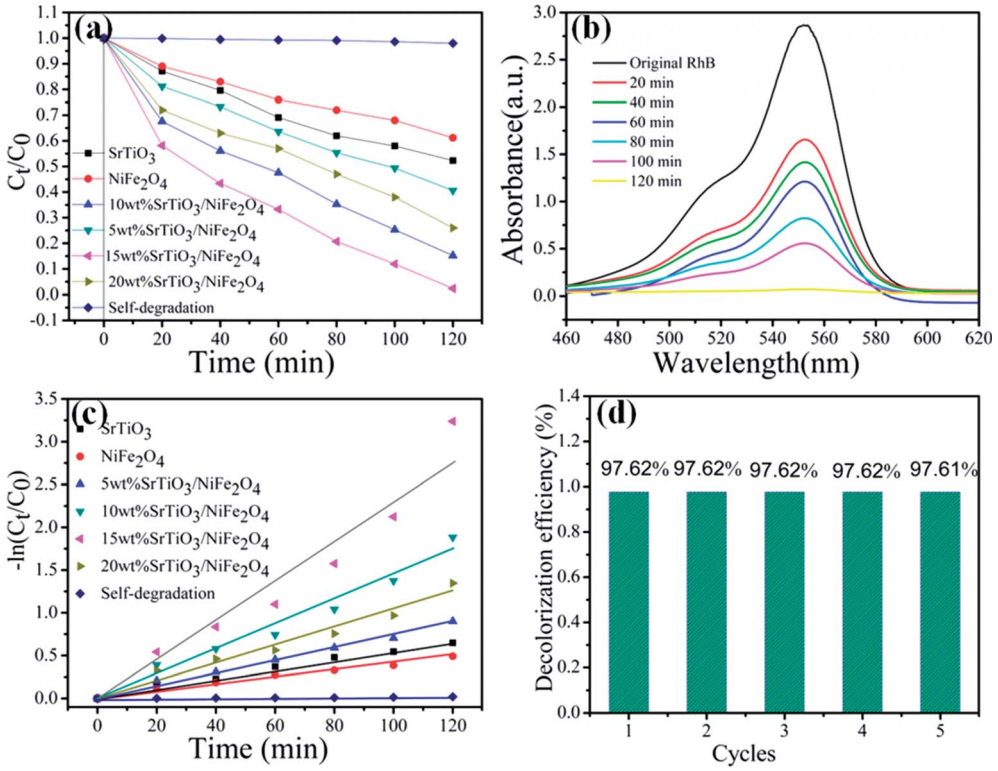

Fig. 8 Photocatalytic degradation of RhB for all samples under simulated solar light illumination (a), absorption spectra of RhB over 15 wt% $SrTiO_3/NiFe_2O_4$ nanocomposites (b), $-\ln(C_t/C_0)$ *vs.* time for photodegradation of RhB by different catalysts (c), cycling degradation rate (d) for RhB of 15 wt% $SrTiO_3/NiFe_2O_4$ nanocomposites under simulated solar light illumination.

rate for 15 wt% $SrTiO_3/NiFe_2O_4$ nanocomposites is approximately 2.5 times and 2 times higher than those for $NiFe_2O_4$ and $SrTiO_3$, respectively, which is superior to the previous studies.[43] The superior photocatalytic performance of 15 wt% $SrTiO_3/NiFe_2O_4$ nanocomposites should be attributed to the strong adsorption abilities and great facilitation of the electron–hole pairs separation. UV-vis spectra are severally observed during degradation of RhB solution under simulated solar light irradiation, as shown in Fig. 8b, revealing the decomposition behaviours of RhB solution over the photocatalysis of 15 wt% $SrTiO_3/NiFe_2O_4$ nanocomposites. The peak intensity of the characteristic absorption at about 554 nm is found to be decreased as reaction time goes on.

To reveal the reaction kinetics of the photo-degradation RhB on different photocatalysts, the degradation rates are calculated using the following pseudo-first-order kinetics (eqn (3))

$$\ln(C_0/C_t) = K_{app}t \quad (3)$$

where C_0, C_t, and K_{app} stand for the initial concentration, the concentration at time t, and the apparent pseudo-first-order rate constant, respectively.[44,45] Fig. 8c shows that $-\ln(C_t/C_0)$ exhibits a good linear relationship with irradiation time and the photocatalytic reaction belongs to the pseudo-first-order reaction. The K_{app}[46] value obtained for $SrTiO_3$, $NiFe_2O_4$, 5 wt% $SrTiO_3/NiFe_2O_4$, 10 wt% $SrTiO_3/NiFe_2O_4$, 15 wt% $SrTiO_3/NiFe_2O_4$ and 5 wt% $SrTiO_3/NiFe_2O_4$ are 5.4×10^{-3}, 4.1×10^{-3}, 7.5×10^{-3}, 1.45×10^{-2}, 2.29×10^{-2} and 1.1×10^{-2} min^{-1}, respectively. Among these composites, the 15 wt% $SrTiO_3/NiFe_2O_4$ nanocomposites display the maximum degradation rate constant.[47] As depicted in Fig. 8d, the dye degradation over the 15 wt% $SrTiO_3/NiFe_2O_4$ nanocomposites show no obvious deterioration after the nanocomposites are reused five times, indicating the excellent stability of the 15 wt% $SrTiO_3/NiFe_2O_4$ nanocomposites photocatalysts.[48]

3.7. Photocatalytic mechanism discussions

In order to better reveal the photocatalytic mechanism, we carried out the trapping experiments on the degradation of RhB under the same conditions. Iso-propyl alcohol (IPA), disodium ethylene-diaminetetraacetate (EDTA-2Na) and benzoquinone (BQ) were used as the scavengers of the hydroxyl radical ($^{\bullet}OH$), holes and superoxide radical ($^{\bullet}O_2^{\bullet-}$), respectively, as shown in Fig. 9. It is found that the addition of BQ or EDTA-2Na to the reaction solution has only a minor suppression on the degradation of RhB and the dye degradation still maintains a high level of 94.72% and 91.78% after 120 min of photocatalysis, respectively, indicating that h^+ and $^{\bullet}O_2^{\bullet-}$ are not the dominant reaction species in the photocatalysis. However, when adding IPA to the reaction solution, the dye degradation is significantly inhibited. Only 24% of the dye is observed to be decolorized on adding IPA, and the decolorization is mainly attributed to the adsorption effect. This implies that the dye degradation is highly correlated with $^{\bullet}OH$.[49]

In order to investigate the migration and separation efficiency of photo-generated charge carriers in as-prepared

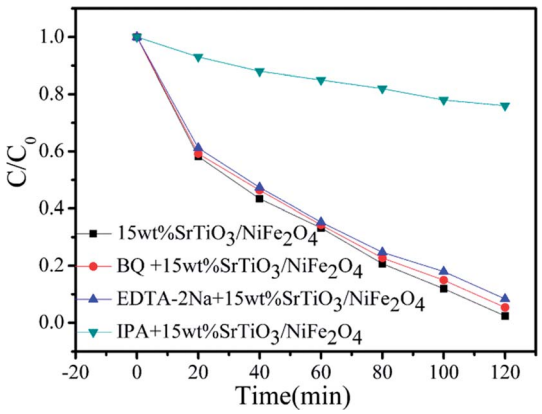

Fig. 9 Reactive species trapping experiments over 15 wt% $SrTiO_3$/$NiFe_2O_4$ nanocomposites.

samples, PL emission spectra for pure $NiFe_2O_4$ and 15 wt% $SrTiO_3$/$NiFe_2O_4$ nanocomposites are shown in Fig. 10. For pure $NiFe_2O_4$, a strong emission peak at 441 nm is observed. A similar PL spectrum was obtained for 15 wt% $SrTiO_3$/$NiFe_2O_4$ nanocomposites, but the overall emission intensity is apparently reduced compared to that of the pure $NiFe_2O_4$. In general, high PL intensity manifests a high electron–hole recombination rate and poor photocatalytic performance.[50] Therefore, the weak emission intensity in 15 wt% $SrTiO_3$/$NiFe_2O_4$ nanocomposites indicates the composition of $SrTiO_3$ and $NiFe_2O_4$ was conducive to prevent the recombination of electrons and holes, which is beneficial for the improvement of photocatalytic performance.

In $SrTiO_3$/$NiFe_2O_4$ nanocomposites, the band positions of $SrTiO_3$ and $NiFe_2O_4$ play an important role in the generation, transference and recombination of photo-generated electron–hole pairs. The band positions of $NiFe_2O_4$ and $SrTiO_3$ are theoretically calculated using the atom's Mulliken electronegativity definition (eqn (4) and (5)):[51]

$$E_{VB} = \chi - E_c + 0.5E_g \quad (4)$$

$$E_{CB} = E_{VB} - E_g \quad (5)$$

where E_{VB} is the valence band (VB) potential, E_{CB} is the conduction band (CB) potential, E_C is the energy of free electrons on the hydrogen scale (*ca.* 4.5 eV), E_g is the band gap energy of the semiconductor, and χ is the absolute electronegativity of the semiconductor.[52,53] Therefore, the E_{VB} and E_{CB} of $NiFe_2O_4$ are calculated to be 2.62 eV and 0.80 eV, respectively, whereas the E_{VB} and E_{CB} of $SrTiO_3$ are about 2.02 eV and −1.13 eV, respectively.

According to the above results, the possible photocatalytic mechanism of the $SrTiO_3$/$NiFe_2O_4$ nanocomposites is illustrated in Fig. 11. When the photocatalyst was irradiation with simulated solar light, the electrons on the VB position are excited to the CB position for both $SrTiO_3$ and $NiFe_2O_4$. The electrons in the CB of $SrTiO_3$ move to the CB of $NiFe_2O_4$ and holes in the VB of $NiFe_2O_4$ transferred to the VB of $SrTiO_3$, and therefore, the electrons–holes pairs get effective separation and avoid recombination. In addition, because the CB value of $NiFe_2O_4$ (0.8 eV) is more positive than the potential of O_2/$^{\bullet}O_2^{-}$ (−0.33 eV *vs.* NHE),[54] the photo-electrons at the CB of $NiFe_2O_4$ are trapped by O_2 to form reactive $^{\bullet}O_2^{-}$ on the photocatalyst surface. $^{\bullet}O_2^{-}$ can react with h^+ to form $HO_2^{\bullet}$ and H_2O_2, and the H_2O_2 reacts with $HO_2^{\bullet}$ to generate hydroxyl ($^{\bullet}OH$) radicals, which cause the degradation of the RhB dye. Compared with the $E^0(^{\bullet}OH/OH^-)$ (1.99 eV *vs.* NHE),[31,55] the VB potential of $SrTiO_3$ (2.02 eV) and $NiFe_2O_4$ (2.62 eV) is more positive, which implies that holes can not react directly with RhB,[56] but the VB holes of $SrTiO_3$ can react with OH^- to produce $^{\bullet}OH$ radicals, $^{\bullet}OH$ is a powerful oxidizing agent and can degrade most pollutants. Additionally, owing to the photo-Fenton reaction, photoelectrons at the CB of $NiFe_2O_4$ can react with H_2O_2 and Fe^{3+} to produce $^{\bullet}OH$ for the oxidation of RhB.[57,58] There action processes can be written as follows:

$$SrTiO_3 + h\nu \rightarrow SrTiO_3(e^-)_{CB} + SrTiO_3(h^+)_{VB} \quad (6)$$

$$NiFe_2O_4 + h\nu \rightarrow NiFe_2O_4(e^-)_{CB} + NiFe_2O_4(h^+)_{VB} \quad (7)$$

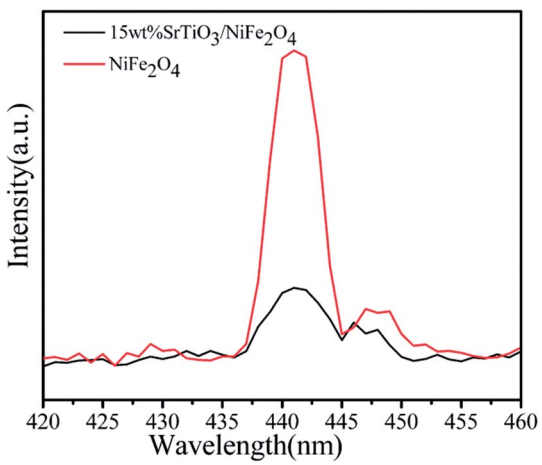

Fig. 10 PL spectra (excited at 325 nm) of pure $NiFe_2O_4$ and 15 wt% $SrTiO_3$/$NiFe_2O_4$ nanocomposites.

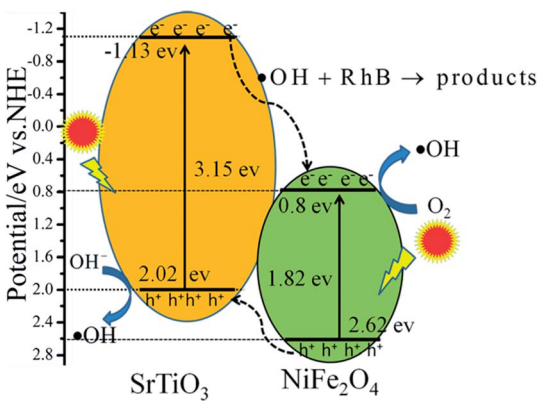

Fig. 11 Schematic illustration of excitation and separation of photo-induced electron–hole pairs for $SrTiO_3$/$NiFe_2O_4$ heterojunction nanocomposites under simulated solar light irradiation.

$$SrTiO_3(e^-)_{CB} + NiFe_2O_4 \rightarrow SrTiO_3 + NiFe_2O_4(e^-)_{CB} \quad (8)$$

$$NiFe_2O_4(e^-)_{CB} + O_2 \rightarrow {}^{\bullet}O_2^- \quad (9)$$

$${}^{\bullet}O_2^- + H^+ \rightarrow HO_2^{\bullet} \quad (10)$$

$$2HO_2^{\bullet} \rightarrow O_2 + H_2O_2 \quad (11)$$

$$H_2O_2 + {}^{\bullet}O_2^- \rightarrow {}^{\bullet}OH + OH^- + O_2 \quad (12)$$

$$SrTiO_3(h^+)_{VB} + OH^- \rightarrow {}^{\bullet}OH \quad (13)$$

$$Fe^{3+} + H_2O_2 + h\nu \rightarrow Fe^{2+} + {}^{\bullet}OH + H^+ \quad (14)$$

$$Fe^{2+} + H_2O_2 + h\nu \rightarrow Fe^{3+} + {}^{\bullet}OH + OH^- \quad (15)$$

4. Conclusion

In summary, novel multifunctional $SrTiO_3/NiFe_2O_4$ nanocomposites were successfully fabricated by coupling $SrTiO_3$ with $NiFe_2O_4$ through a two-step route. It demonstrates that the $SrTiO_3/NiFe_2O_4$ heterojunction structure is composed of $NiFe_2O_4$ nanoparticles adhered to the $SrTiO_3$ spheres. The heterojunction established in the composite material accelerates the process of electron–hole pair separation and boosts the photo-Fenton reaction. Among all the samples, the 15 wt% $SrTiO_3/NiFe_2O_4$ nanocomposites exhibit a powerful light response, excellent room temperature ferromagnetism, and the best photoactivity for degradation of RhB organic pollutants under simulated solar light irradiation. Furthermore, according to experimental results, the possible mechanism of improved photocatalytic activity is also proposed.

Conflicts of interest

The authors declare no competing financial interest.

Acknowledgements

This work was supported by the National Natural Science Foundation of China (61107055) and the Specialized Research Fund for the Doctoral Program of Jiangsu University of Technology (KYY17011).

Notes and references

1 J. Liu, Y. Liu, N. Y. Liu, Y. Z. Han, X. Zhang, H. Huang, Y. Lifshitz, S. T. Lee, J. Zhong and Z. H. Kang, *Science*, 2015, **347**, 970–974.
2 M. A. Shannon, P. W. Bohn, M. Elimelech, J. G. Georgiadis, B. J. Marinas and A. M. Mayes, *Nature*, 2008, **452**, 301–310.
3 A. Ahuja and K. M. Mosalam, *Energy and Buildings*, 2017, **153**, 448–460.
4 S. Piskunov, O. Lisovski, J. Begens, D. Bocharov, Y. F. Zhukovskii, M. Wessel and E. Spohr, *J. Phys. Chem. C*, 2015, **119**, 18686–18696.
5 C. T. Cherian, J. Sundaramurthy, M. V. Reddy, P. S. Kumar, K. Mani, D. Pliszka, C. H. Sow, S. Ramakrishna and B. V. R. Chowdari, *ACS Appl. Mater. Interfaces*, 2013, **5**, 9957–9963.
6 H. Song, L. P. Zhu, Y. G. Li, Z. R. Lou, M. Xiao and Z. Z. Ye, *J. Mater. Chem. A*, 2015, **3**, 8353–8360.
7 T. H. Yu, W. Y. Cheng, K. J. Chao and S. Y. Lu, *Nanoscale*, 2013, **5**, 7356–7360.
8 M. Dhiman, A. Goyal, V. Kumar and S. Singhal, *New J. Chem.*, 2016, **40**, 10418–10431.
9 H. S. Kim, D. J. Kim, B. S. Kwak, G. B. Han, M. H. Um and M. Kang, *Chem. Eng. J.*, 2014, **243**, 272–279.
10 R. J. Elias and A. L. Waterhouse, *Food Chem.*, 2010, **58**(3), 1699–1707.
11 H. Y. Ji, X. C. Jing, Y. G. Xu, J. Yan, H. P. Li, Y. P. Li, L. Y. Huang, Q. Zhang, H. Xu and H. M. Li, *RSC Adv.*, 2015, **5**, 57960–57967.
12 J. Zeng, T. Song, M. X. Lv, T. T. Wang, J. Y. Qin and H. P. Zeng, *RSC Adv.*, 2016, **6**, 54964–54975.
13 D. D. Lv, D. F. Zhang, X. Y. Liu, Z. G. Liu, L. Y. Hu, X. P. Pu, H. Y. Ma and D. C. Li, *Sep. Purif. Technol.*, 2016, **158**, 302–307.
14 P. Xiong, Y. S. Fu, L. J. Wang and X. Wang, *J. Chem. Eng.*, 2012, **195–196**, 149–157.
15 H. Y. Zhu, R. Jiang, Y. Q. Fu, R. R. Li, J. Yao and S. T. Jiang, *Appl. Surf. Sci.*, 2016, **369**, 1–10.
16 L. Zhang and W. L. Jiao, *J. Alloys Compd.*, 2013, **581**, 11–15.
17 J. Zhou, L. Yin, K. Zha, H. R. Li, Z. Y. Liu, J. X. Wang, K. Duan and B. Feng, *Appl. Surf. Sci.*, 2016, **367**, 118–125.
18 M. N. Ha, F. Zhu, Z. F. Liu, L. C. Wang, L. Y. Liu, G. Z. Lu and Z. Zhao, *RSC Adv.*, 2016, **6**, 21111–21118.
19 D. Yang, Y. Y. Sun, Z. W. Tong, Y. H. Nan and Z. Y. Jiang, *J. Hazard. Mater.*, 2016, **312**, 45–54.
20 O. Ruzimuradov, M. Hojamberdiev, C. Fasel and R. Riedel, *J. Alloys Compd.*, 2017, **699**, 144–150.
21 D. N. Bui, J. Mua, L. Wang, S. Z. Kang and X. Q. Li, *Appl. Surf. Sci.*, 2013, **274**, 328–333.
22 X. Chen, P. F. Tan, B. H. Zhou, H. G. Dong, J. Pan and X. Xiong, *J. Alloys Compd.*, 2015, **647**, 456–462.
23 S. Kumar, S. Tonda, A. Baruah, B. Kumarb and V. Shanker, *Dalton Trans.*, 2014, **43**, 16105–16114.
24 B. Modak and S. K. Ghosh, *J. Phys. Chem. C*, 2015, **119**, 7215–7224.
25 J. J. Guo, S. X. Ouyang, P. Li, Y. J. Zhang, T. Kakoa and J. H. Ye, *Appl. Catal., B*, 2013, **134–135**, 286–292.
26 T. Kanagaraj and S. Thiripuranthagan, *Appl. Catal., B*, 2017, **207**, 218–232.
27 Q. Zhang, Y. Huang, S. Q. Peng, Y. F. Zhang, Z. X. Shen, J. J. Cao, W. K. Ho and S. C. Lee, *Appl. Catal., B*, 2017, **204**, 346–357.
28 P. Jing, J. L. Du, J. B. Wang, W. Lan, L. N. Pan, J. N. Li, J. W. Wei, D. R. Cao, X. L. Zhang, C. B. Zhao and Q. F. Liu, *Nanoscale*, 2015, **7**, 14738–14746.
29 G. X. Tong, Y. Liu, T. Wu, C. L. Tong and F. F. Du, *J. Mater. Chem. C*, 2015, **3**, 5506–5515.
30 T. Kanagaraj and S. Thiripuranthagan, *Appl. Catal., B*, 2017, **207**, 218–232.

31 Z. M. He, Y. M. Xia, B. Tang, X. F. Jiang and J. B. Su, *Mater. Lett.*, 2016, **184**, 148–151.
32 E. Y. Guo and L. W. Yin, *J. Mater. Chem. A*, 2015, **3**, 13390–13401.
33 H. Y. Zhu, R. Jiang, S. H. Huang, J. Yao, F. Q. Fu and J. B. Li, *Ceram. Int.*, 2015, **41**, 11625–11631.
34 P. Xiong, Y. Fu, L. Wang and X. Wang, *Chem. Eng. J.*, 2012, **195–196**, 149–157.
35 Z. Y. Yu, L. F. Chen and S. H. Yu, *J. Mater. Chem. A*, 2014, **2**, 10889–10894.
36 H. S. Kim, D. J. Kim, B. S. Kwak, G. B. Han, M. H. Um and M. Kang, *Chem. Eng. J.*, 2014, **243**, 272–279.
37 V. Subramanian, R. K. Roeder and E. E. Wolf, *Ind. Eng. Chem. Res*, 2006, **45**, 2187–2193.
38 L. J. Di, H. Yang, T. Xian and X. J. Chen, *Materials*, 2017, **10**(1118), 1–11.
39 O. Ruzimuradov and M. Hojamberdiev, *J. Alloys Compd.*, 2017, **699**, 144–150.
40 L. Wang, Z. J. Wang, D. H. Wang, X. C. Shi, H. Song and X. Q. Gao, *Solid State Sci.*, 2014, **31**, 85–90.
41 A. Ren, C. B. Liu, Y. Z. Hong, W. D. Shi, S. Lin and P. Li, *Chem. Eng. J.*, 2014, **258**, 301–308.
42 J. T. Deng, L. Liu, T. J. Niu and X. S. Sun, *Appl. Surf. Sci.*, 2017, **403**, 531–539.
43 X. Zhao, H. Yang, Z. Cui, R. Li and W. Feng, *Mater. Technol.*, 2017, **32**, 870–880.
44 Y. Q. Wang, X. F. Cheng, X. T. Meng, H. W. Feng, S. G. Yang and C. Sun, *J. Alloys Compd.*, 2015, **632**, 445–449.
45 L. Zhang, X. Zhang, Y. Q. Huang, C. L. Pan, J. S. Hu and C. M. Hou, *RSC Adv.*, 2015, **5**, 30239–30247.
46 S. F. Wang, H. Yang, T. Xian and X. Q. Liu, *Catal. Commun.*, 2011, **12**, 625–628.
47 H. Yang, J. X. Zhang, G. J. Lin, T. Xian and J. L. Jiang, *Adv. Powder Technol.*, 2013, **24**, 242–245.
48 M. Zhang, H. Yang, T. Xian, Z. Q. Wei, J. L. Jiang, Y. C. Feng and X. Q. Liu, *J. Alloys Compd.*, 2011, **509**, 809–812.
49 F. Wang, H. Yang and Y. C. Zhang, *Mater. Sci. Semicond. Process.*, 2018, **73**, 58–66.
50 R. He and C. H. Yin, *Acta Biomater.*, 2017, **53**, 355–366.
51 T. Xian, H. Yang, L. J. Di and J. F. Dai, *J. Alloys Compd.*, 2015, **622**, 1098–1104.
52 Q. Wang, Q. J. Guo, L. P. Wang and B. Li, *Dalton Trans.*, 2016, **45**, 17748–17758.
53 C. M. Su, *J. Hazard. Mater.*, 2017, **322**, 48–84.
54 S. Maiti, S. Pal and K. K. Chattopadhyay, *CrystEngComm*, 2015, **17**, 9264–9295.
55 G. Y. He, J. J. Ding, J. G. Zhang, Q. L. Hao and H. Q. Chen, *Ind. Eng. Chem. Res*, 2015, **54**, 2862–2867.
56 T. Xian, H. Yang, J. F. Dai, Z. Q. Wei, J. Y. Ma and W. J. Feng, *Mater. Lett.*, 2011, **65**, 1573–1575.
57 R. Sharma, S. Bansal and S. Singhal, *RSC Adv.*, 2015, **5**, 6006–6018.
58 C. X. Zheng, H. Yang, Z. M. Cui, H. M. Zhang and X. X. Wang, *Nanoscale Res. Lett.*, 2017, **12**, 608.